Effect of dimensionality and spin-orbit coupling on charge-density-wave transition in 2H-TaSe_{2}

Yizhi Ge and Amy Y. Liu

Phys. Rev. B **86**, 104101 — Published 4 September 2012

DOI: 10.1103/PhysRevB.86.104101

Effect of dimensionality and spin-orbit coupling on charge-density-wave transition in 2H-$TaSe_2$

Yizhi Ge and Amy Y. Liu
Department of Physics, Georgetown University, Washington, DC 20057

A first-principles investigation of the charge-density-wave (CDW) instability in bulk and single-layer 2H-$TaSe_2$ is presented, focusing on the origin of the CDW instability, the role of the interlayer interactions, and the effect of spin-orbit coupling. While interlayer interactions and spin-orbit coupling have a nontrivial effect on the electronic structure and Fermi surface, the CDW instability is predicted to remain robust, with little or no change in the ordering wave vector. This is in contrast to the closely related 2H-$NbSe_2$ material, where the CDW wave vector depends on dimensionality. The results are analyzed in terms of the interplay between the momentum dependence of the electron-phonon coupling and that of the electronic response function.

PACS numbers: 71.45.Lr, 63.20.kd, 63.22.Dc, 71.70.Ej

I. INTRODUCTION

The driving mechanism behind charge-density-wave (CDW) formation has been a long-standing question in solid-state physics. Explanations of the CDW instability have variously emphasized Fermi-surface nesting,[1] van Hove singularities,[2] and electron-phonon coupling,[3,4] among others. A criterion[5] for a stable CDW phase characterized by a wave vector $\mathbf{q}$ is

$$\frac{4|g_{\mathbf{q}\nu}|^2}{\hbar\omega^{bare}_{\mathbf{q}\nu}} \geq \frac{1}{\chi_{\mathbf{q}}} + (2U_{\mathbf{q}} - V_{\mathbf{q}}), \qquad (1)$$

where ν is a phonon branch index, $|g_{\mathbf{q}\nu}|^2$ is the average of the squared electron-phonon matrix element, $\omega^{bare}_{\mathbf{q}\nu}$ is the unrenormalized phonon energy, $\chi_{\mathbf{q}}$ is the dielectric susceptibility of the electrons, and $U_{\mathbf{q}}$ and $V_{\mathbf{q}}$ are the average Coulomb and exchange interaction of electrons. This condition expresses a balance between the lowering of the electronic energy and the increase in the lattice energy upon CDW formation. In the Peierls' model for noninteracting electrons in 1D, the CDW transition results from the divergence of the electronic susceptibility χ_q due to perfect nesting when $q = 2k_F$, where k_F is the Fermi wave vector. In this case, the instability is fundamentally electronic in origin and directly related to nesting. However, in the case of layered quasi-2D CDW materials, the role of Fermi-surface nesting and purely electronic origins for the CDW instability have increasingly been called into question.[3,4,6–8] In Ref. 4, for example, Johannes and Mazin pointed out that the degree of Fermi-surface nesting is measured by the *imaginary* part of the electronic response function, while it is the *real* part that appears in Eq. (1). Indeed, first-principles investigations of layered CDW materials such as 1T-TaS_2,[6] 1T-$TaSe_2$,[7] and 2H-$NbSe_2$[3,8] have found no correlation between strong nesting vectors and the CDW ordering vector.

In the layered transition-metal dichalcogenide CDW systems, the origin of the CDW instability can be probed by varying the interlayer separation, as different mechanisms are expected to respond differently. Consider, for example, the 2H polytypes of $NbSe_2$, $TaSe_2$, and TaS_2, which have bulk CDW phases with similar ordering wave vectors of $\mathbf{Q}_{cdw} \approx \mathbf{b_1}/3$, where $\mathbf{b_1}$ is a primitive in-plane reciprocal lattice vector of the normal or undistorted structure. In $NbSe_2$, pressure decreases the CDW transition temperature, eventually suppressing the transition completely.[9] In $TaSe_2$, the normal-to-incommensurate-CDW transition temperature has a weak positive pressure coefficient, while the incommensurate-to-commensurate transition temperature decreases with pressure.[10] The response to intercalation has also been mixed. In some cases (*e.g.*, silver intercalated $NbSe_2$[11]) the CDW transition temperature increases, while in others (*e.g.*, sodium doped TaS_2[12]) it decreases. In addition, in some systems the CDW structure at the surface differs from that in the bulk. The room temperature surface phonon spectrum of 2H-$TaSe_2$,[13] for example, has an anomaly at $\mathbf{q} = \mathbf{b_1}/2$ rather than at $\mathbf{Q}_{cdw}$, where the anomaly is located in the bulk spectrum.[14] Furthermore, scanning tunneling microscopy studies show that the CDW structure at the surface of Ag-intercalated 2H-$NbSe_2$ is described by a $\sqrt{13} \times \sqrt{13}$ supercell instead of the 3×3 bulk CDW structure.[11]

Recently, mechanical and chemical exfoliation techniques similar to those used to make graphene have been applied to layered dichalcogenides to produce few- and single-layer samples.[15,16] This offers a clean way to assess the role of dimensionality and interlayer interactions on the CDW transition in these materials. Experiments on thin multi-layer 2H-TaS_2 patches, for example, find no evidence for a CDW transition.[17] On the other hand, a density-functional investigation of 2H-$NbSe_2$ predicts that compared to the bulk, the CDW phase in monolayers should be more stable and be characterized by a different $\mathbf{Q}_{cdw}$ than the bulk.[18] The change in $\mathbf{Q}_{cdw}$ is attributed to the momentum dependence of the electron-phonon matrix elements.

In this paper, we investigate the structural, electronic, and vibrational properties of bulk and single-layer 2H-$TaSe_2$ using first principles methods. The origin of the CDW instability and the effect of dimensionality are ex-

plored. We find that the CDW instability remains robust upon removal of the interlayer interactions in 2H-$TaSe_2$, with little or no change in the ordering wave vector, even though the wave-vector dependences of the electron-phonon interaction and of the electronic response function both vary with the strength of interlayer interactions. We also find that the Fermi surfaces of both the bulk and single-layer materials are very sensitive to spin-orbit coupling, yet the phonon spectra, including the location of unstable modes, are not significantly impacted. The robustness of the ordering wave vector in 2H-$TaSe_2$ is explained through the interplay between the two sides of Eq. (1). These results also provide a basis for a more general discussion about the variety of behaviors exhibited by the 2H dichalcogenides as interlayer interactions are varied.

II. COMPUTATIONAL METHOD

The calculations were performed within density functional theory (DFT) using the Quantum ESPRESSO suite of codes.[19] The exchange-correlation interaction was treated with the local density approximation (LDA) using the Perdew Zunger parameterization of the correlation energy.[20] For most of the results presented, the interaction between electrons and ionic cores was described by scalar relativistic ultrasoft pseudopotentials.[21] The energy cut-off for the plane-wave basis set was 35 Ry. A $18\times 18\times 6$ uniform mesh of $\mathbf{k}$-points was used to sample the Brillouin zone, and the Vanderbilt-Marzari Fermi smearing method was used to accelerate convergence.[22] Unless otherwise noted, a smearing parameter of $\sigma = 0.02$ Ry was used. Phonon dispersion curves and electron-phonon coupling parameters were calculated using density functional perturbation theory.[23] The double Fermi-surface averages of electron-phonon matrix elements were calculated using the tetrahedron method on grids of up to $90\times 90\times 12$ $\mathbf{k}$ points. To investigate the effect of spin-orbit coupling, some fully relativistic calculations were carried out with norm-conserving pseudopotentials[24] requiring an energy cut off of 72 Ry.

III. DESCRIPTION OF STRUCTURES

The high-temperature bulk structure of 2H-$TaSe_2$ consists of stacked Se-Ta-Se trilayer units.[25] Each atomic sheet within a trilayer is close packed, and the sheets are aligned so that each Ta site is at the center of a trigonal prism formed by Se sites. The distance between trilayer units is large compared to the spacing between sheets in a trilayer. The primitive cell contains two trilayers with their metal sites aligned vertically and their trigonal prisms rotated 60° with respect to each other, as shown in Fig. 1. The single-layer structure is defined as one trilayer unit.

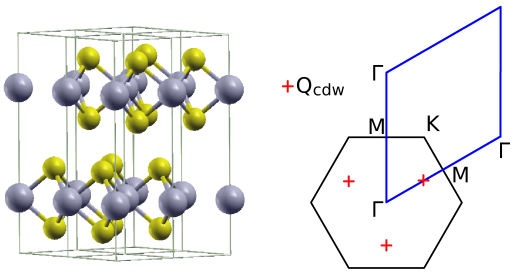

FIG. 1: (Color online) Crystal structure and Brillouin zone of 2H-$TaSe_2$. The large spheres (gray) correspond to Ta atoms and the small spheres (yellow) represent Se atoms. The bulk 2H structure contains two trilayers per unit cell, while the single-layer structure corresponds to an isolated trilayer unit. High-symmetry points in the $q_z = 0$ plane of the hexagonal Brillouin zone are labeled, as well as a triplet of ordering vectors $\mathbf{Q}_{cdw}$.

In the bulk material, an incommensurate charge density wave forms at about 122 K, with an ordering wave vector of $\frac{(1-\delta)}{3}\mathbf{b_1}$, where $\delta \approx 0.02$. In a second transition, near 90 K, δ becomes zero, leading to a commensurate structure. In fact, the structure is characterized by a triplet of equivalent wave vectors that are oriented 120° with respect to each other in the Brillouin zone, resulting in a 3×3 supercell in real space. In each supercell, six Ta atoms surrounding a central Ta site displace roughly radially inward, forming a seven-atom cluster.[25,26]

IV. RESULTS AND DISCUSSION

A. Structural instability

The structure of bulk 2H-$TaSe_2$ was optimized, resulting in lattice parameters $a = 3.39$ Å, $c = 12.23$ Å, and $z_{Se} = 0.135$. With the exception of the separation between trilayer units, the underestimation of which is expected within the LDA, the structure is in good agreement with experimental findings.[25] For the single-layer calculations, the position of Se atoms was optimized at the bulk value for the in-plane lattice constant and with $c = 15$ Å, ensuring at least 11 Å of vacuum between adjacent trilayers.

The phonon dispersion curves calculated for bulk 2H-$TaSe_2$ are shown in Fig. 2(a). The width over which electronic states near the Fermi level are smeared was varied in order to examine the effect of electronic temperature on the stability of the structure. At the electronic temperature of $\sigma = 0.02$ Ry, two low-lying branches display anomalous dips along the Γ-M line. Along this line, both of these branches involve longitudinal displacements of Ta atoms. As the electronic temperature is lowered, the softening increases and at $\sigma = 0.01$ Ry, the longitudinal acoustic branch is found to be unstable over an extended region of the Brillouin zone. The instability first occurs

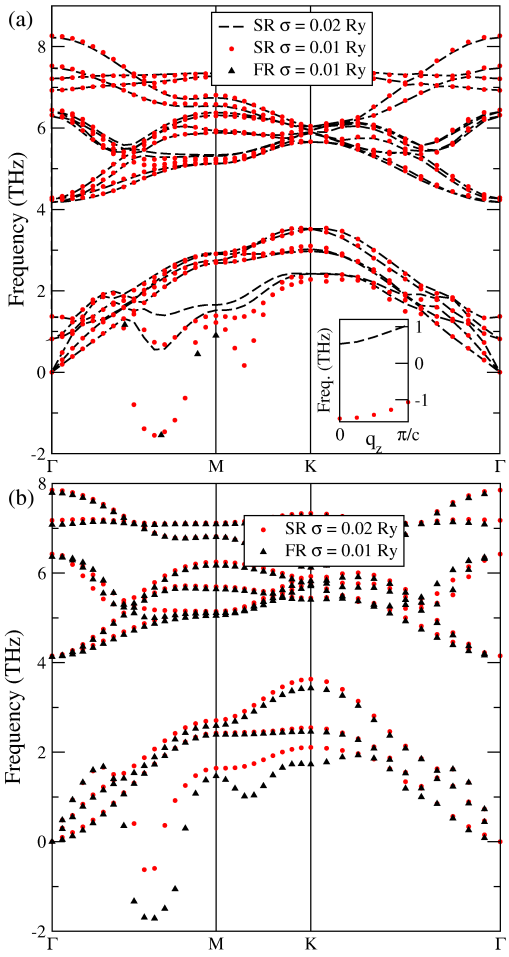

FIG. 2: Phonon dispersion of 2H-$TaSe_2$. (a) Bulk results are shown for three cases: scalar relativistic (SR) dispersion curves at two electronic temperatures and fully relativistic (FR) results along Γ-M for the unstable acoustic branch. (b) Single-layer dispersion curves are plotted for both scalar relativistic and fully relativistic calculations. Negative values indicate imaginary frequencies. The inset in (a) shows the q_z dispersion of the soft branch along the line that projects onto the CDW ordering vector.

close to the experimentally observed CDW wave vector, which is at two thirds along the Γ-M line. The inset in Fig. 2(a) displays the out-of-plane dispersion of the soft acoustic branch along the line with an in-plane projection of $\mathbf{q}_\parallel = \mathbf{b}_1/3$, showing that the instability is strongest in the $q_z = 0$ plane.

Figure 2(b) shows the calculated phonon dispersion curves for single-layer 2H-$TaSe_2$. As in the bulk, acoustic modes that involve in-plane motion of Ta atoms soften and become unstable as the electronic temperature is lowered. Results are shown only for an electronic temperature where the structure is dynamically unstable. The instability occurs at approximately the same wave vector as in the bulk, but the anomaly has a narrower, more cusp-like shape, though softening still occurs over an extended region of the Brillouin zone.

TABLE I: Comparison of bulk and single-layer (1L) CDW parameters. Scalar relativistic and fully relativistic results are presented for the total energy (per formula unit) of the 3×3 CDW structure relative to that of the undistorted structure, ΔE, and for the fractional change in the distance from the center Ta site to its nearest neighbors in the CDW supercell, $\Delta R/R$.

	Bulk SR	1L SR	Bulk FR	1L FR	Bulk Expt[25]
ΔE (mRy/f.u.)	-0.08	-0.22	-0.12	-0.10	N/A
ΔR/R	-1.1%	-1.9%	-1.1%	-1.6%	-1.3%

Results of fully relativistic (FR) calculations are plotted as triangles in Fig. 2. For the single layer, phonon wave vectors were sampled on the same grid used in the scalar relativistic (SR) calculations. Only the soft acoustic branch shows significant dependence on spin-orbit coupling. The location of the instability remains essentially unchanged upon inclusion of the spin-orbit interaction, but the region of the instability broadens and is more similar to the bulk result in Fig. 2(a). In light of these results for the single layer, we limited our fully relativistic calculations for the bulk to selected wave vectors, primarily along the Γ-M direction. As shown in Fig. 2(a), the low-lying branch along Γ-M in the bulk is very similar whether or not spin-orbit coupling is included.

Since the existence of imaginary phonon frequencies indicates dynamical instabilities but does not reveal what the stable structure is, we have carried out total-energy calculations using the 3×3 supercell for the commensurate CDW phase. Holding the lattice constants fixed, the atomic positions in the bulk and in the single layer were relaxed after Ta atoms were slightly displaced from their high-symmetry positions. In both systems, seven-atom Ta clusters formed, as observed in neutron scattering.[25] The results of the supercell calculations, both scalar relativistic and fully relativistic, are summarized in Table I. The amplitude of the CDW distortion is predicted to be larger in the single layer than in the bulk, but the energy gained from the distortion is similar for the two structures. This is in contrast to the case of 2H-$NbSe_2$, where calculations predict a much larger energy gain for the single layer than for the bulk.[18] These results are qualitatively consistent with the observation that near ambient pressure, the pressure derivative of the normal-to-incommensurate transition temperature has been measured to be very weakly positive for $TaSe_2$[10] and negative for $NbSe_2$.[9]

B. Electronic structure

As discussed in Ref. 4, spin-orbit coupling affects the bulk 2H-$TaSe_2$ bands near the Fermi level in a nontrivial way, and it is necessary to include spin-orbit coupling

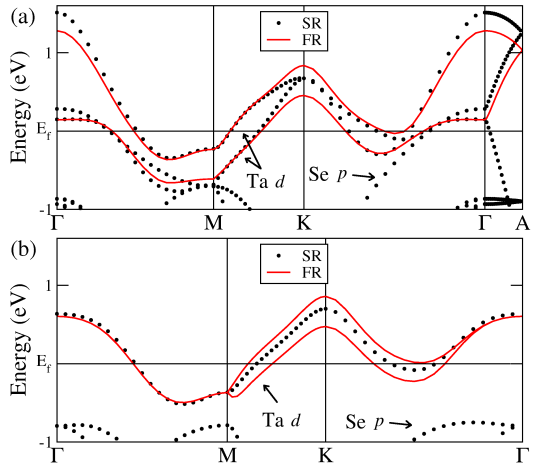

FIG. 3: Calculated electronic band structure of (a) bulk and (b) single-layer 2H-$TaSe_2$. The Fermi level is set to zero. Solid lines show the spin-orbit-split fully relativistic Ta d bands. The fully relativistic bulk bands were calculated at the experimental value of the c lattice constant.

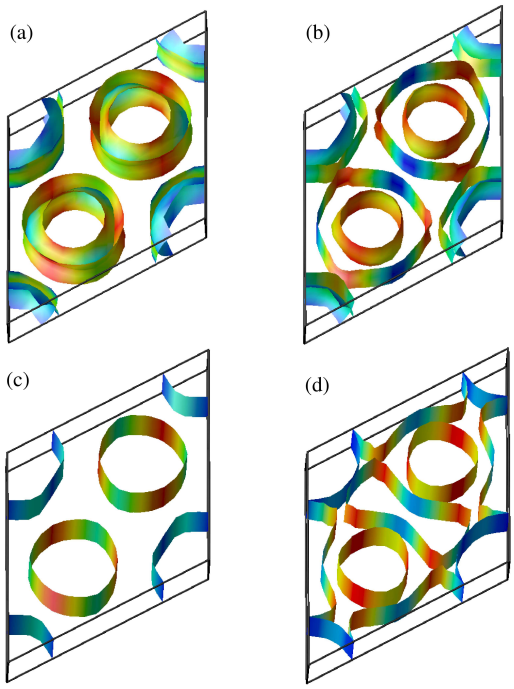

FIG. 4: (Color online) Calculated Fermi surfaces arising from Ta d bands in 2H-$TaSe_2$. (a) Bulk Fermi surface in the scalar-relativistic approximation. (b) Bulk Fermi surface calculated fully relativistically, showing spin-orbit splitting of bands in the $k_z = \pi/2$ plane. (c) Single-layer Fermi surface in the scalar-relativistic approximation. (d) Single-layer Fermi surface calculated fully relativistically, with new sheets appearing as a result of the spin-orbit interaction. The Γ point lies at the corners of the zone shown. The K-centered sheets have strong $d_{xy}/d_{x^2-y^2}$ character (red), particularly near the Γ-K lines, while the Γ-centered sheets have weak $d_{xy}/d_{x^2-y^2}$ character (blue).

to bring the calculated Fermi surface in alignment with results from angle-resolved photoelectron spectroscopy measurements (ARPES).[27] Since the single-layer structure is noncentrosymmetric, one might anticipate spin-orbit coupling to have an even more significant effect on the band splittings and the Fermi surface in the single layer.

The band structures of bulk and single-layer 2H-$TaSe_2$ are shown in Fig. 3, with and without spin-orbit coupling. In the single-layer scalar-relativistic calculation, a single band (doubly degenerate due to spin), primarily of Ta d character, crosses the Fermi level. The corresponding Wannier function localized at each Ta site has d_{z^2} symmetry near the Ta atom, but tails of d_{xy} or $d_{x^2-y^2}$ character extending out towards neighboring Ta sites.[26] This band gives rise to two roughly cylindrical Fermi sheets, with one centered around Γ and one centered around K, as shown in Fig. 4(c). The states on the Γ-centered hole sheet project strongly onto Ta d_{z^2} orbitals, while those on the K-centered hole sheet have large contributions from $d_{xy}/d_{x^2-y^2}$ orbitals. On both types of sheets, the in-plane $d_{xy}/d_{x^2-y^2}$ character is strongest near the Γ-K lines.

When the inter-trilayer distance is decreased and the trilayers are rotated relative to each other to form the bulk, the Ta d band at the Fermi level broadens and splits into a bonding and antibonding pair. The splitting is largest at the Γ point, while the two bands remain degenerate on the $k_z = \pi/c$ plane since the intracell-bonding/intercell-antibonding orbitals are equivalent to the intracell-antibonding/intercell-bonding ones.[3] In additional, the Se p_z band, which lies below the Fermi level in the single layer, also broadens and splits into a bonding and antibonding pair in the bulk. The antibonding p_z band is pushed up in energy and crosses the Fermi level. Increasing the c lattice constant from the LDA value to the experimental value reduces the width of the Se p_z band so that it remains below the Fermi level, as found in photoemission experiments.[27] Figure 4(a) shows the four Fermi sheets associated with the Ta d bands in the scalar-relativistic approximation: two centered around the Γ-A line, and two around the K-H line. All four Ta d hole sheets show considerable warping along the k_z axis due to interlayer interactions, with concentric sheets having maximum separation in the $k_z = 0$ plane and coinciding in the $k_z = \pi/c$ plane. Nevertheless, the projections of in-plane d orbitals on the Fermi sheets have weak k_z dependence and are similar overall to the single-layer case.

Since the bulk 2H structure is inversion symmetric, the fully relativistic bands remain two-fold degenerate, and the number of Ta d bands crossing the Fermi level does not change. Four Fermi sheets arise from the Ta d bands, but as shown in Fig. 4(b), the sheets around the K-H line show less dispersion along k_z because the spin-orbit interaction splits the degeneracy in the $k_z = \pi/c$ plane. While the Fermi surface in Fig. 4(b) does not have the M-centered dog-bone-shaped electron pockets observed in ARPES studies,[27] a small downward shift of

the calculated Fermi level by about 20 meV eliminates the Fermi-level crossing of one of the d bands along the Γ-K direction, bringing the theoretical and experimental Fermi surfaces into better agreement. As discussed in Ref. 4, although the Fermi surface *looks* very different when this slight shift in the Fermi level is applied, properties such as the nesting function (discussed below) do not change appreciably.

Unlike the bulk, a single layer of 2H-$TaSe_2$ lacks a center of inversion. Thus with spin-orbit coupling, the doubly degenerate Ta d band at the Fermi level splits into two nondegenerate bands (except in the vertical mirror plane containing the Γ-M line.) As a result, new electron sheets, which have a dog-bone shape, appear in the fully-relativistic Fermi surface, as shown in Fig. 4(d).

C. Origin of the instability and effect of interlayer interactions

So far we have shown that the CDW instability occurs at nearly the same wave vector for bulk and single-layer 2H-$TaSe_2$, with and without spin-orbit coupling, even though the Fermi surface topologies differ significantly in these different cases. This strongly suggests that the instability is not closely tied to the topology of the Fermi surface. The Fermi surface nesting function is related to the imaginary part of the noninteracting susceptibility in the static limit,

$$\lim_{\omega\to 0} \chi''_{\mathbf{q}}(\omega)/\omega = \sum_{\mathbf{k}jj'} \delta(\epsilon_{\mathbf{k}j} - E_F)\delta(\epsilon_{\mathbf{k}+\mathbf{q}j'} - E_F). \quad (2)$$

It was shown in Ref. 4 that the nesting factor for bulk 2H-$TaSe_2$ (including spin-orbit effects) is sharply peaked at the K point in the Brillouin zone, and is otherwise relatively flat (expect near Γ, where it diverges). Though the detailed structure of the nesting function varies in the four cases in Fig. 4, the general features are similar, and in no case is the nesting function peaked near $\mathbf{Q}_{cdw}$. Geometric nesting of the Fermi surface can therefore be ruled out as the driving mechanism for the CDW instability in either the bulk or the single-layer material.

Figure 5(a) shows the wave-vector dependence of the electron-phonon coupling parameter in bulk 2H-$TaSe_2$, calculated at $\sigma = 0.02$ Ry, where the structure is dynamically stable, and limited to the acoustic branch that becomes unstable as the electronic temperature is lowered. The coupling of this phonon branch to electrons is moderately large over an extended region of the Brillouin zone, and is particularly large near $\mathbf{Q}_{cdw}$, at about 1/3 along the M-K line (which we will call $\mathbf{Q}'$), and along the line connecting neighboring $\mathbf{Q}_{cdw}$ points that map onto each other under a 60° rotation.

The structure of $\lambda_{\mathbf{q}\nu}$ in momentum space is qualitatively different from what we previously found for the 1T polymorphs of $TaSe_2$ and TaS_2. In the 1T materials, $\lambda_{\mathbf{q}\nu}$ was calculated to be sharply peaked at the experimentally observed CDW vector, so it was clear that the momentum dependence of the electron-phonon coupling was determining the ordering vector. In 2H-$TaSe_2$, the electron-phonon coupling is large at many wave vectors, so from the plot of $\lambda_{\mathbf{q}\nu}$ alone, it would be difficult to predict the $\mathbf{q}$ vector at which the lattice first becomes unstable. This suggests that we need to consider the right-hand side of Eq. (1). Figure 5(b) shows the wave-vector dependence of the real part of the electronic susceptibility,

$$\chi'_{\mathbf{q}} = \sum_{\mathbf{k}jj'} \frac{f(\epsilon_{\mathbf{k}+\mathbf{q}j'}) - f(\epsilon_{\mathbf{k}j})}{\epsilon_{\mathbf{k}j} - \epsilon_{\mathbf{k}+\mathbf{q}j'}}, \quad (3)$$

where $f(\epsilon)$ is the Fermi-Dirac function. The susceptibility has a broad maximum near $\mathbf{Q}_{cdw}$ and lines of minima along M-K and Γ-K. Hence while the CDW instability is driven by strong interactions between electrons and

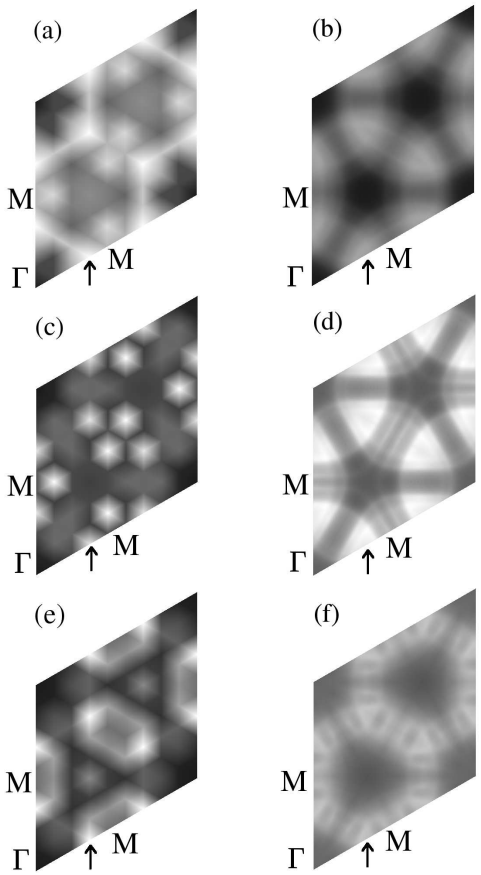

FIG. 5: Wave-vector dependence of electron-phonon coupling and electronic susceptibility in bulk and single-layer 2H-$TaSe_2$. Panels (a), (c), and (e) show $\lambda_{\mathbf{q}\nu}$ and for the soft acoustic branch in the SR bulk ($\sigma = 0.02$ Ry), the SR single layer ($\sigma = 0.03$ Ry), and the FR single layer ($\sigma = 0.2$ Ry), respectively. Black denotes $\lambda_{\mathbf{q}\nu} = 0$, while white represents the maximum value, which is different in each case. Panels (b), (d), and (f) show the real part of the susceptibility $\chi'_{\mathbf{q}}$ per formula unit calculated for the SR bulk, the SR single layer, and the FR bulk, respectively, using a common gray scale. Arrows indicate $\mathbf{Q}_{cdw}$.

phonons that give rise to enhanced electronic screening of certain phonon modes, we find that the wave vector at which the strongest softening occurs depends not just on $\lambda_{\mathbf{q}\nu}$, but rather on the interplay between the $\mathbf{q}$ dependence of the electron-phonon interaction and that of the electronic response function.

Figure 5(c) and (d) show $\lambda_{\mathbf{q}\nu}$ and $\chi'_{\mathbf{q}}$ for a single layer of 2H-$TaSe_2$. The electron-phonon coupling parameter is dominated by sharp peaks near $\mathbf{Q}_{cdw}$ and $\mathbf{Q}'$ (1/3 the way from M to K), with $\lambda_{\mathbf{q}\nu}$ at these points being more than twice as large as in the bulk. One the other hand, the wave-vector dependence of $\chi'_{\mathbf{q}}$ in the single layer is similar to that in the bulk, though there is an overall enhancement in the values due to the narrowing of the d band as the interaction between trilayers weakens. The global maximum in $\lambda_{\mathbf{q}\nu}$ lies on the M-K line, but this line lies in a shallow trench in the susceptibility function. At $\mathbf{Q}_{cdw}$, both $\lambda_{\mathbf{q}\nu}$ and $\chi'_{\mathbf{q}}$ are close to their maximum values, resulting in the softening and instability seen at this point in Fig. 2(b). Thus even though the electron-phonon coupling as a function of wave vector is rather different in the single layer as compared to the bulk, the interplay with the electronic response function selects out the same ordering wave vector in both cases.

Figure 5(e) and (f) show $\lambda_{\mathbf{q}\nu}$ and $\chi'_{\mathbf{q}}$ for a single layer with spin-orbit coupling. The electron-phonon coupling is large at $\mathbf{Q}_{cdw}$ and $\mathbf{Q}'$ as in the scalar-relativistic case, but the region over which the function is large is extended. On the other hand the response function develops fine structure, with a narrower peak near $\mathbf{Q}_{cdw}$. Both the coupling and the response function are maximal at $\mathbf{Q}_{cdw}$, again selecting this wave vector for the instability.

We consider now the factors that lead to a strong interaction for a particular phonon mode and how they depend on the strength of interlayer interactions. The branch- and wave-vector-dependent $\lambda_{\mathbf{q}\nu}$ is proportional to an average of the square of the electron-phonon matrix element,

$$g(\mathbf{k}j;\mathbf{k}+\mathbf{q}j';\mathbf{q}\nu) = \sqrt{\frac{\hbar}{2M\omega_{\mathbf{q}\nu}}}\langle \mathbf{k}j|\hat{\epsilon}_{\mathbf{q}\nu}\cdot\delta V_{SCF}|\mathbf{k}+\mathbf{q}j'\rangle, \tag{4}$$

where $\hat{\epsilon}_{\mathbf{q}\nu}\cdot\delta V_{SCF}$ is the self-consistent change in the potential due to displacements following the phonon eigenvector $\hat{\epsilon}_{\mathbf{q}\nu}$. The average of $|g|^2$ is taken as in Eq. 2, where $\mathbf{k}$ and $\mathbf{k}+\mathbf{q}$ are constrained to the Fermi surface. In both the bulk and single-layer materials, the low-lying phonon branch that becomes unstable involves primarily in-plane motion of the Ta atoms (and a combination of in-plane and out-of-plane motion of the Se atoms). These motions couple strongly to electronic states that have charge concentrated in the Ta planes. Thus we expect that substantial matrix elements for this phonon branch will arise at phonon wave vectors $\mathbf{q}$ that span points on the Fermi surface dominated by in-plane Ta d electronic states. On the Fermi surfaces in Fig. 4, each K-centered sheet has three regions with large in-plane d projection. These "hot zones" lie near the Γ-K lines on the K-centered sheets [and on the dog-bone sheets in panel Fig. 4(d)]. Although the Fermi surfaces differ, in each case, the phonon wave vectors with strong electron-phonon coupling in Fig. 5 connect "hot zones" on the corresponding Fermi surfaces. However, not all vectors that connect in-plane states show up as strong peaks in the plots of the coupling strength since the matrix element depends on how strongly a particular phonon displacement pattern impacts those electronic states.

For the single layer in the scalar relativistic approximation, there are three inequivalent ways to connect pairs of "hot zones", and for each pair, a range of wave vectors spans points in these regions. The intrasheet spanning vectors are centered around $\mathbf{Q}_{cdw}$, while one set of intersheet connections is centered around $\mathbf{Q}'$. Introducing interactions between trilayers warps the Fermi surface along k_z, so the phonon wave vectors that connect in-plane states on the Fermi surface now depend on k_z. This explains how the sharp peaks in the single-layer $\lambda_{\mathbf{q}\nu}$ at just two inequivalent wave vectors [Fig. 5(c)] evolve into weaker peaks and an extended region of relatively large $\lambda_{\mathbf{q}\nu}$ in the bulk [Fig. 5(a)].

In the single layer, spin-orbit coupling doubles the K- and Γ-centered sheets, and the outer sheets around these points touch to form the M-centered dog bones. Considering only phonon wave vectors parallel to $\mathbf{b_1}$, there are now three inequivalent ways to connect "hot zones" on the K-centered and dog-bone sheets, with overlapping ranges. The vector $\mathbf{Q}_{cdw}$ lies near the center of this range, and connects in-plane states on the K-sheet to those on the dog-bone sheet. This accounts for the broader region of phonon softening that is still centered around the same point, as seen in Fig. 2(b), when the spin-orbit effect is taken into account. In the case of the bulk, spin-orbit coupling reduces the warping of the K sheets, which tends to narrow the region of softening, but this is counteracted by a wider range of phonon wave vectors that connect in-plane states due to the expansion of one sheet and the shrinking of the other. The result is that the region of softening in the bulk is not as strongly affected by spin-orbit coupling as in the single layer.

As noted above, just because a phonon wave vector connects "hot spots" on the Fermi surface doesn't necessarily mean it has a large electron-phonon coupling parameter. To examine this, it is useful to adopt a real-space picture. Consider for example a 3×1 supercell for the bulk, which has a periodicity consistent with the ordering vector $\mathbf{Q}_{cdw}$. The Ta d states originally at $\mathbf{k}=\pm\mathbf{Q}_{cdw}$ (about 0.3 eV below the Fermi level) fold back to the Γ point in the supercell. The displacement of ions according to the eigenvectors of the longitudinal acoustic mode compresses (or expands) regions in which the charge associated with one (or the other) of these states is concentrated, leading to an upward (or downward) shift in the band and a significant coupling matrix element g. For other wave vectors, the displacement pattern has less impact on the volume in which charge is concentrated, resulting in weaker coupling. This

real-space description is conceptually similar to the local bonding picture developed by Whangbo and Canadell in Ref. 28. To explain the tendency for 2H d^1 transition metal dichalcogenides to undergo a 3×3 modulation, they used an extended Hückel model to show that the experimentally determined distortion pattern changes the net overlap population of metal-metal bonds, leading to a lowering of the total energy.

V. CONCLUSIONS

This work shows that density functional theory provides an accurate description of the CDW instability in bulk 2H-$TaSe_2$ and predicts the instability to persist in single-layer 2H-$TaSe_2$, at the same or nearly the same wave vector. The instability is found to be due to strong coupling of in-plane Ta d states near the Fermi level with phonons that involve in-plane Ta displacements. However, since the electron-phonon coupling is large at multiple phonon vectors, the momentum dependence of the electron-phonon coupling alone is not sufficient for determining the wave vector at which the instability manifests. Instead, the momentum-space structure of the dielectric response function must also be considered. This is in contrast to previous findings for 1T-$TaSe_2$, where $\lambda_{\mathbf{q}\nu}$ was sharply peaked only near $\mathbf{Q}_{cdw}$.

Although geometric nesting of the Fermi surface is found to be irrelevant to the instability, the shape of the Fermi surface nevertheless plays a role in that it affects the wave-vector dependence of the electron-phonon coupling. A necessary (but not sufficient) condition for large coupling is that the phonon momentum vector connects "hot zones" on the Fermi surface, where the in-plane character of the electronic states is large. Since the interlayer interaction affects the k_z dispersion of the Fermi surface, and the spin-orbit interaction can change the Fermi surface topology and even the number of Fermi sheets, the momentum dependence of $\lambda_{\mathbf{q}\nu}$ changes as the strength of these interactions is varied. Thus it is somewhat surprising that the phonon instability is calculated to occur at or about the same wave vector in the bulk and in the single layer, with or without spin-orbit coupling. By considering the structure of $\chi'_{\mathbf{q}}$ together with that of $\lambda_{\mathbf{q}\nu}$, we are able to understand this result.

Our prediction that the CDW manifests at the same (or nearly the same) wave vector in single-layer and bulk 2H-$TaSe_2$ is in contrast to 2H-$NbSe_2$, where calculations indicate that the ordering vector depends on dimensionality.[18] Due to the smaller mass of the metal atom, spin-orbit effects are not expected to be as important in $NbSe_2$ as in $TaSe_2$. Comparing the scalar relativistic Fermi surfaces for the single-layer structures, we notice a difference in the shape of the K-centered sheet. This sheet has a more triangular cross section in single-layer $NbSe_2$, which decreases the length of the vector that spans regions of in-plane states on this sheets. This could explain, at least in part, the shift of the instability to a smaller wave vector in single-layer $NbSe_2$.

Our results are also in contrast to observations of a shifted surface-phonon anomaly in 2H-$TaSe_2$.[13] Given that the location and degree of phonon softening is determined by multiple factors, each of which reacts differently to changes in the strength of interlayer interactions and spin-orbit coupling, it is plausible that the reduced symmetry at the surface affects the ordering vector. Further work is needed, however, to fully understand the difference between the single layer and the surface. More generally, with the interplay of different factors, we expect that differences in the electronic structure of isostructural, isoelectronic materials, doping effects in intercalated materials, and changes in symmetry could impact the ordering vector or even the stability of a CDW phase. So while this work has focused on 2H-$TaSe_2$, it helps to elucidate the variety of behaviors observed in the CDW dichalcogenides when interlayer interactions are tuned.

Acknowledgments

This research was supported by the NSF through Grant No. DMR-1006605 and through TeraGrid resources provided by the Texas Advanced Computing Center.

[1] J. A. Wilson, F. J. DiSalvo, and S. Mahajan, Phys. Rev. Lett. **32**, 882 (1974).
[2] T. M. Rice and G. K. Scott, Phys. Rev. Lett. **35**, 120 (1975).
[3] M. D. Johannes, I. I. Mazin, and C. A. Howells, Phys. Rev. B **73**, 205102 (2006).
[4] M. D. Johannes and I. I. Mazin, Phys. Rev. B **77**, 165135 (2008).
[5] S. K. Chen and V. Heine, J. Phys. F **3**, 795 (1973).
[6] A. Y. Liu, Phys. Rev. B **79**, 220515(R) (2009).
[7] Y. Ge and A. Y. Liu, Phys. Rev. B **82**, 155133 (2010).
[8] F. Weber, S. Rosenkranz, J.-P. Castellan, R. Osborn, R. Hott, R. Heid, K.-P. Bohnen, T. Egami, A. H. Said, and D. Reznik, Phys. Rev. Lett. **107** 107403 (2011).
[9] C. W. Chu, V. Diatschenko, C. Y. Huang, and F. J. DiSalvo, Phys. Rev. B **15**, 1340 (1977).
[10] C. W. Chu, L. R. Testardi, F. J. DiSalvo, and D. E. Moncton, Phys. Rev. B **14**, 464 (1976).
[11] B. Koslowski, W. Xu, B. Blackford, and M. H. Jericho, Phys. Rev. B **54**, 11706 (1996).
[12] L. Fang, Y. Wang, P. Y. Zou, L. Tang, Z. Xu, H. Chen, C. Dong, L. Shan, and H. H. Wen, Phys. Rev. B **72**, 014534 (2005).
[13] G. Benedek, G. Brusdeylins, C. Heimlich, L. Miglio, J. G. Skofronick, J. P. Toennies, and R. Vollmer, Phys. Rev. Lett. **60**, 1037 (1988).

[14] D. E. Moncton, J. D. Axe, and F. J. DiSalvo, Phys. Rev. Lett. **34**, 734 (1975).
[15] K. S. Novoselov, D. Jiang, F. Schedin, T. J. Booth, V. V. Khotkevich, S. V. Morozov, and A. K. Geim, Proc. Nat. Acad. Sci. **102**, 10451 (2005).
[16] J. Coleman *et al.*, Science **331**, 568 (2011).
[17] A. Ayari, E. Cobas, O. Ogundadegbe, and M. S. Fuhrer, J. Appl. Phys. **101**, 014507 (2007).
[18] M. Calandra, I. I. Mazin, and F. Mauri, Phys. Rev. B **80**, 241108(R) (2009).
[19] http://www.quantum-espresso.org.
[20] J. P. Perdew and A. Zunger, Phys. Rev. B **23**, 5048 (1981).
[21] D. Vanderbilt, Phys. Rev. B **41**, 7892 (1990).
[22] N. Marzari, D. Vanderbilt, A. De Vita, and M. C. Payne, Phys. Rev. Lett. **82**, 3296 (1999).
[23] S. Baroni, S. de Gironcoli, A. Dal Corso, and P. Giannozi, Rev. Mod. Phys. **73**, 515 (2001).
[24] A. M. Rappe, K. M. Rabe, E. Kaxiras, and J. D. Joannopoulos, Phys. Rev. B **41**, 1227 (1990).
[25] D. E. Moncton, J. D. Axe and F. J. DiSalvo, Phys. Rev. B **16**, 801 (1977).
[26] R. L. Barnett, A. Polkovnikov, E. Demler, W.G. Yin, and W. Ku, Phys. Rev. Lett. **96**, 026406 (2006).
[27] K. Rossnagel, E. Rotenberg, H. Koh, N. V. Smith, and L. Kipp, Phys. Rev. B **72**, 121103 (2005).
[28] M. H. Whangbo and E. Canadell, J. Am. Chem. Soc. **114**, 9587 (1992)